Nano Research
2022, 15(1): 145–152

ISSN 1998-0124 CN 11-5974/O4
https://doi.org/10.1007/s12274-021-3382-3

Research Article

Docking MOF crystals on graphene support for highly selective electrocatalytic peroxide production

Xiaofeng Huang[1], Peter Oleynikov[1], Hailong He[1], Alvaro Mayoral[1], Linqin Mu[2], Feng Lin[2], and Yue-Biao Zhang[1] (✉)

[1] *School of Physical Science and Technology, ShanghaiTech University, Shanghai 201210, China*
[2] *Department of Chemistry, Virginia Tech, Blacksburg, VA 24061, USA*

Received: 8 January 2021 / **Revised:** 31 January 2021 / **Accepted:** 1 February 2021

ABSTRACT

Tailoring the reaction kinetics is the central theme of designer electrocatalysts, which enables the selective conversion of abundant and inert atmospheric species into useful products. Here we show a supporting effect in tuning the electrocatalytic kinetics of oxygen reduction reaction (ORR) from four-electron to two-electron mechanism by docking metalloporphyrin-based metal–organic frameworks (MOFs) crystals on graphene support, leading to highly selective peroxide production with faradaic efficiency as high as 93.4%. A magic angle of 38.1° tilting for the co-facial alignment was uncovered by electron diffraction tomography, which is attributed to the maximization of π–π interaction for mitigating the lattice and symmetry mismatch between MOF and graphene. The facilitated electron migration and oxygen chemisorption could be ascribed to the supportive effect of graphene that disperses of the electron state of the active center, and ultimately regulates rate-determining step.

KEYWORDS

metal–organic frameworks, nanocomposites, support effect, oxygen reduction reaction, peroxide selectivity

1 Introduction

Hydrogen peroxide (H_2O_2) served as a versatile feedstock for multiple industrial purposes is mass-produced via the so-called anthraquinone oxidation process in which the organics reacts with gaseous hydrogen under demanding condition [1]. For its feasibility and on-site supply purpose, electrochemical production of H_2O_2 has long been pursued [2–6], calling for the tailored understanding and design of the electrocatalysts [7, 8]. Considerable efforts have been made to modulate the electronic structures of catalysts via strain [9], alloying [10], and doping [11]. Interfacial interactions induced from a supportive substrate represent a fruitful strategy for manipulating the electron status of nanocomposites [12–17]. Indeed, this strategy leads to materials whose performance is dictated by the axiom, "the whole is greater than the sum of its parts" [18, 19].

As emerging crystalline porous materials, metal–organic frameworks (MOFs) have shown their prospect in electrochemistry, featuring the deliberate control of reticular architectures and the ingenious manipulation of the electronic properties to optimize/interplay the resulting activity, selectivity and efficiency [20–26]. However, the bottleneck arising from the poor electronic conductivity of MOFs calls for the elaborative crystal interface between MOF and conductive supports/substrates [13]. To overcome the difficulty of significant lattice mismatch, self-assembled monolayer (SAM) has been utilized to graft MOFs on substrate through layer-by-layer method. The alkyl organic feature of SAM renders it a resistant layer in terms of electron transfer [27, 28]. Solution-phase epitaxial growth places MOFs directly on substrates, which might have explicit alignment of MOF on limited synthetic substrates such as Ag, Pd, and $Cu(OH)_2$ [29–31]. To tailor the electrocatalytic performance, we sought to implement the solution-phase growth of MOFs on graphene materials to maximize their contacts. Specifically, we have docked a grid-layered MOFs, comprising cobaltopophyrin linkers and paddle-wheel building units, on graphene supports (Fig. 1). With the doping and functionality of graphene optimized, the electrocatalytic performance and reaction kinetics in the oxygen reduction reactions (ORR)

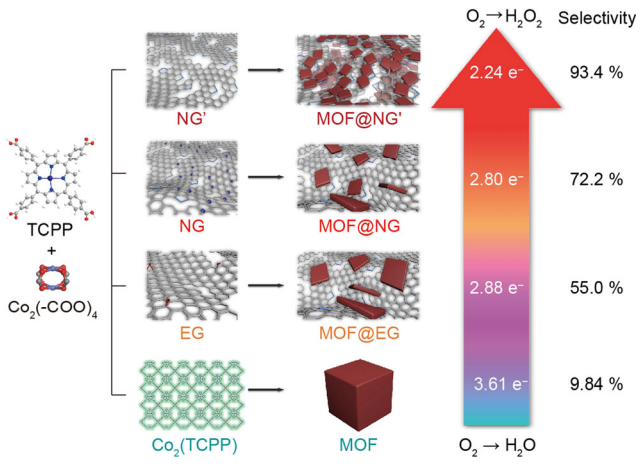

Figure 1 Schematic illustration of steering the ORR pathways and boosting the peroxide selectivity via the manipulation of the docking alignments of the layered cobalt-porphyrin MOF [Co_2(TCPP); TCPP = Cobalt(II) tetracarboxylphenyl porphyrin] on various graphene supports including **EG** (electro-chemical exfoliated graphene), **NG** (nitrogen-doped graphene), and **NG'** (high-power sonicated nitrogen-doped graphene) to form MOF-graphene nanocomposites.

Address correspondence to zhangyb@shanghaitech.edu.cn

were therefore optimized and steered towards two-electron pathway, showing high selectivity toward peroxide production. The mechanism of the kinetic control is attributed to the dispersed electron state of the active centers that facilitated the detachment of O_2^- intermediate. Such supporting effect of graphene is originated from co-facial docking orientation of MOF and graphene that possess a twist angle of ~ 38° overcoming huge lattice mismatch and symmetry mismatch. This work features optimized supporting effect in the tailor-designed reaction kinetics and electron state for target-oriented electrocatalysis.

2 Results and discussion

2.1 Oxygen reduction behavior of graphene supported MOF

Observed by scanning electron microscopy (SEM), as-synthesized layered cobalt-porphyrin MOFs was ca. 20–30 μm in size and tetragonal prismatic shaped crystals in appearance through solvothermal reaction, as shown in Fig. S1 in the Electronic Supplementary Materials (ESM). The **MOF** adopts a square-grid layered structure (**sql** net) by stitching the CoTCPP linkers with the $Co_2(COO)_4$ paddle-wheel clusters (Figs. S2 and S3, and Table S1 in the ESM). Perfectly-defined tetragonal electron diffraction pattern rendered its good crystallinity, which is also in line with the simulated pattern (Figs. S3(c) and S3(d) in the ESM). Reconstruction of the *hk*0 plane indicates its finely-ordered in-plane structure (Figs. S3(e) and S3(f) in the ESM). However, the observed diffusive reconstructed pattern and reciprocal rod along the *c* direction (Figs. S3(g) and S3(h) in the ESM) implied its irregular stacking of single MOF layer onto one another. Nevertheless, a family of such MOF structures are of ease in controlled synthesis and have been widely used in constructing nanocomposites [32–34]. In such solvothermal reaction, addition of certain types graphene supports, namely **EG** (electrochemically exfoliated graphene), **NG** (nitrogen-doped graphene), and **NG'** (high-power sonicated nitrogen-doped graphene) yield MOF-graphene nanocomposites with well-retained MOF structure verified from the powder X-ray diffraction patterns (PXRD) shown in Fig. S4 in the ESM.

Investigated through cyclic voltammetry (CV), the ORR behaviors of graphene supported MOF displayed intense reduction peaks in O_2-purged 0.5 M H_2SO_4 electrolyte than that of pristine MOF (Fig. 2(a); Fig. S5 in the ESM), implying the supportive contribution from graphene. Hydrodynamic voltammograms at various rotation speeds were recorded to elucidate the role of graphene supports in ORR electrochemical kinetics (Fig. 2(b); Fig. S6 in the ESM). At 1,600 rpm, mass-transfer-corrected Tafel slopes in Fig. 2(c) were tilted from > 120 mV·dec^{-1} (all MOF-graphene nanocomposites except **MOF@NG'**), around 90 mV·dec^{-1} (**MOF**) and ultimately to 58 mV·dec^{-1} (**MOF@NG'**). The corresponding kinetics were gradually changing from a single electron transfer-controlled step to a O_2 chemisorption-controlled step [34].

The gradual tuning of the electrode kinetics indicates a change in the underlying ORR performance. In the absence of graphene supports, pristine MOF transferred 3.61 electrons to O_2, which corresponds to a H_2O_2 selectivity of only 19.7% (Fig. 2(b)). The ability for four-electron reduction behavior is likely arising from the stepwise 2-electron process judging from their reduction behavior in H_2O_2 (Fig. S7 in the ESM). The peroxide yield on **MOF@EG** and **MOF@NG** was moderately improved to 56%–59% suggesting the ratio for the two-electron pathway starts to increase. Specifically on **MOF@NG'**, it exhibited the number of electrons transferred per O_2 reached 2.24, which corresponding to a peroxide yield of 88.2% based on rotating ring-disk voltammetry results (Fig. 2(e)), uncovering its dominant two-electron pathway. When it was further subject to constant potential electrolysis of O_2 at 0.4 V vs. reversible hydrogen electrode (RHE), the concentration of H_2O_2 showed a steady increment over 6 h, giving the highest Faradaic efficiency of 93.4% for **MOF@NG'** (Fig. 2(d); Fig. S8 in the ESM). Such peroxide selectivity is higher than those of the oxidized carbon nanotube and defect contained carbon [35], nitrogen-doped graphene [36], boron nitride [37], and other reported electrocatalysts (Table 1), and is comparable to mildly oxidized

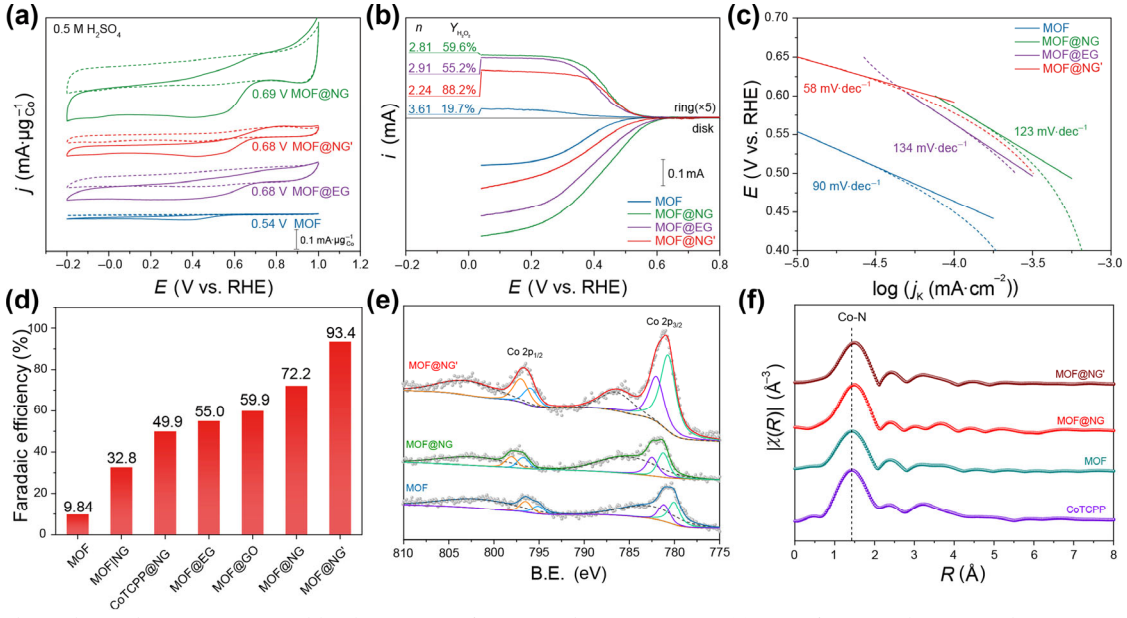

Figure 2 Electrochemical ORR activities and local structures of MOF-graphene composites. (a) CVs of **MOF** and MOF-graphene nanocomposites in N_2(dash line)/O_2(solid line) purged 0.5 M H_2SO_4 solution with a scan rate of 10 mV·s^{-1}. (b) Rotating ring-disk voltamogramms of MOF-graphene nanocomposites in O_2 purged 0.5 M H_2SO_4 solution with a scan rate of 5 mV·s^{-1} at 1,600 rpm. (c) Tafel slopes of the MOF-graphene nanocomposites. (d) Faradaic efficiencies of peroxide formation on MOF-graphene nanocomposite. (e) High resolution XPS of Co 2p core level. (f) k^3-space EXAFS of **MOF** and MOF-graphene nanocomposites.

Table 1 Limiting current density (j_{lim}), onset potential (E_{onset}), number of electrons transferred (n) and faradaic efficiencies (H_2O_2 FE, determined from constant potential electrolysis) from this work compared with reported two-electron electrocatalysts

Catalyst	j_{lim} (mA·cm^{-2})	E_{onset} (V vs. RHE)	n	H_2O_2 FE (%)	Ref.
MOF@NG'	**0.816**	**0.50**	**2.2**	**93.4**	**This work**
MOF@NG	**1.812**	**0.57**	**2.8**	**72.2**	
Mesoporous nitrogen-doped carbon	~ 3.5	~ 0.73	2.52–2.72	65–73	[38]
Polypyrrole/anthraquinones composite film	(-)	~ 0.19	2.02	(-)	[39]
TiN nanoparticle (12 nm)	~ 0.4	0.7	(-)	~70	[40]
Ju-NG	~ 1.8	~ 0.57	1.9–2.1	(-)	[41]
NC900	~ 4	0.8	2.1	(-)	[42]
C(Pt)/C	~1.8	0.57	3.2–3.3	41	[43]
Mesoporous nitrogen-doped carbon	~ 2.6	0.4	~ 2	93–95	[44]
Nitrogen doped graphene	~ 0.8	~ 0.67	2.5	(-)	[45]
MOF(Fe/Co)+SP	~ 4	~ 0.67	2–3	(-)	[46]
GOQDs	~ 2.7	~ 0.66	2.21–2.24	(-)	[47]
RGO/Au	~ 0.5	0.8	~ 2	(-)	[48]
Fe(meso-tetraphenylporphyrin)	~ 0.15	0.3	(-)	58	[49]
Fe/pyrolzed polyimide	~ 1.3	0.7	2.4	~ 60	[50]
Mesoporous Nitrogen-Doped Carbon	~ 3	~ 0.4	~ 2	65.15	[51]
Co-POC-O	(-)	0.84	(-)	87.7	[52]
Co_1-NG(O)	~ 3	~ 0.75	(-)	~ 82	[53]
Co-N-C	2.9	~ 0.75	~ 2.4	80	[54]
MOF NSs-300	3	0.75	~ 2	99	[55]
Mn-O/N@NCs-50	~ 1.3	~ 0.3	2,5	74	[56]
NCMK3IL50_800T	~ 1.8	0.55	2.1	95–98	[57]
PEI50CMK3_800T	~ 1.5	0.49	2.05	95.2–98.5	[58]
5-Ni_3(HITP)$_2$	~ 1.7	~ 0.7	(-)	80	[59]
N-mFLG-8	~ 3	~ 0.72	< 2.1	95	[60]
Pt_1Ag_1/C	(-)	~ 0.55	2.1	> 90	[61]
G/CDs	0.4	0.85	2.3	82	[62]
Exfoliated 2H-$MoTe_2$	1.9	0.56	(-)	93	[63]

graphene [52], hetero-atom doped mesoporous carbon [51, 64–66], graphitized carbon nanohorns [67], and carbon dots [68]. Since sole **NG'** in constant potential electrolysis do not produce H_2O_2 (Fig. S8 in the ESM), the promotion of H_2O_2 selectivity in **MOF@NG'** probably correlated with the nanocomposite interface.

Additionally, the electrocatalytic turnover of oxygen to H_2O_2 can be further optimized by the graphene substrate. As **NG** showed the least R_{ct} (Table S2 in the ESM), it enabled **MOF@NG** to have the highest electron conductivity (see Fig. S9 and Table S3 in the ESM) along with a higher amount of O_2 chemisorption (Fig. S10 in the ESM). They could be further optimized by means of increasing the electrochemically active surface area and decreasing the R_{ct} via increasing the concentration of **NG** (Fig. S12 and Table S4 in the ESM). Consequently, it gained a satisfactory ORR mass activity outperforming even some of the reported Pt/Pd alloy catalysts (Table S5 in the ESM) [69–72]. Meanwhile, the highest turnover number (TON) of 36.7 for H_2O_2 production is obtained (Fig. S8 in the ESM). Reticular assembly of CoTCPP is crucial for increasing the TON, as the molecular assembly, **CoTCPP@NG**, only displayed a steep drop in H_2O_2 Faradaic efficiency. However, the enhancement in the ORR performance is probably not correlated to the surface area of these nanocomposites (Fig. S11 in the ESM). Thereby, the observed graphene supporting-dependent ORR selectivity and catalytic turnover suggest possible electronic interaction upon graphene substrate incorporation.

2.2 Electron state modulated by supported graphene

As neither **NG** nor **NG'** exhibited selective oxygen reduction to H_2O_2, local electronic states at the Co(II) active center of MOF-graphene composite interface were characterized by a combined X-ray photoelectron spectroscopy (XPS), Raman spectroscopy, and X-ray absorption spectroscopy (XAS) study to probe the MOF-graphene interaction. In the Co 2p high-resolution spectra (Fig. 2(e)), the Co $2p_{3/2}$ peak can be deconvoluted into two peaks in the binding energy (B.E.) region between 780–782 eV, indicating the co-existence of Co-N_4 unit and $Co_2(COO)_4$ paddlewheel unit [73, 74]. Notably, the Co $2p_{3/2}$ moiety peaks in **MOF@NG** and **MOF@NG'** shifted to the higher B.E. region, and the Co-N interatomic distance was increased compared to CoTCPP and **MOF** according to the first peak from the Fourier transformed k^3-space extended X-ray absorption fine structure spectra (EXAFS) (Fig. 2(f). These explicitly showed that the electronic density of Co(II) was dispersed by the nitrogen doped graphene supports [75-79]. Such finding was further supported by the downshift of graphitic and pyrrolic peaks in **MOF@NG** and **MOF@NG'** compared to those of **NG** and **NG'** in the N 1s spectra (Fig. S13 in the ESM) and downshifts of certain typical bands of the MOF in the Raman spectroscopy of the MOF-graphene nanocomposites (Fig. S14 and Table S6 in the ESM). Also, the more intense peak at 7,679 eV in the pre-edge region of the Co-*K* edge (Fig. S15 in the ESM) implying the distortion of ligand field of Co(II) in **MOF@NG'** [80] also supports our hypothesis. Several works

reported that oxygen moieties like epoxy groups are responsible for the high peroxide selectivity for Co-N_4 electrocatalysts [81]. We cannot rule out such possibility, since oxygen contents existed in the **EG**, **NG**, and **NG'** substrates (Fig. S16 in the ESM). Judging from the neglectable peroxide TON for **NG'** in the constant potential electrolysis, we conjecture that the oxygen contents do not play significant role in enhancing the peroxide selectivity in our case. We anticipate surface-sensitive operando techniques like surface-enhanced Raman spectroscopy [82] would uncover the in-depth understanding of the peroxide production mechanism on **MOF@NG'**.

The interfacial structure for the nanocomposites were further characterized to rationalize electron density dispersion. SEM images of MOF-graphene displayed diversified MOF morphologies among the nanocomposite samples (Fig. 3(a); Fig. S17 in the ESM). In both of their **NG** and **EG** nanocomposites, MOF sheets with thickness at ~ 1 μm in relatively larger size (5-10 μm) were found (Figs. S17(a) and S17(b) in the ESM), where random docking orientations were generally observed. Contrastedly, co-facially aligned orientation of MOF sheets was observed on the **NG'** support with decent uniformity (Fig. 3(a); Figs. S18 and S19 in the ESM). Selected area electron diffraction (SAED) were also performed to verify this orientation. We were able to obtain both sets of diffraction spots belonging to MOF (tetragonal) and graphene (hexagonal) lattices, respectively (Fig. 3(b)). Magnification of this diffraction further showed a set tetragonal spots around the spot of **NG'**, as it was shown in Fig. 3(c). This secondary diffraction phenomenon confirmed that MOF sheets were actually co-facially docked onto rather than randomly anchored to nitrogen-doped graphene support. Additional results from scanning transmission electron microscopic (STEM) images displayed clear tetragonal fringes of MOF docked on **NG'** (Fig. 3(d); Fig. S20(a) in the ESM). Fast Fourier transformation (FFT) of the whole region led to a similar emergence of both patterns further supports the proposed co-facial aligned regime. Surprisingly, we also observe an intersection angle of ~ 38.1° between two sets of diffraction (Fig. 3(e); Fig. S20(b) in the ESM), which may be related to the twist angle compensating their mismatch in lattice and symmetry (tetragonal vs. hexagonal). Based on these evidences, a unit cell matching for the alignment between MOF and graphene is thus proposed and illustrated in Fig. 3(f). Compared with the reported FDM-23 or Ni-CAT-1 on single layer graphene system [83-85], the current CoTCPP MOF-nitrogen doped graphene system have overcome the unmatched crystal symmetry and lattice constant.

Structure of graphene support in terms of morphology and functionality is a crucial factor for realizing such varied docking orientation. Although **EG**, **NG**, and **NG'** all possessed 2-4 layers of graphene (Figs. S21-S23 in the ESM), **NG'** was cleaved into much smaller sizes of ~ 1 μm via high-power ultrasonication compared to an average of 5-10 μm for **NG** (Fig. S24 in the ESM). Additionally, the functionality densities increased in the order of **EG**, **NG**, and **NG'** judging from their Raman spectra (Fig. S25 in the ESM). Oxygen content in the graphene poses deleterious effect for the orientation, as MOF aligned randomly in **MOF@EG** and exhibited much more inferior crystallinity and morphology in **MOF@GO** (Fig. S6(c) in the ESM). The type of nitrogen dopant, however, plays a critical role in aligning MOF onto graphene. With nearly the same nitrogen occupancy (3.95% for **NG** vs. 4.05% for **NG'**), pyrrolic and graphitic-type nitrogen are found dominant in **NG'** from XPS investigation (Figs. S13 and S16 in the ESM) [86, 87]. They may serve as orientation modulator for the formation of co-facial aligned MOF-graphene nanocomposite, thus maximizing their interface for the modulation to the active site.

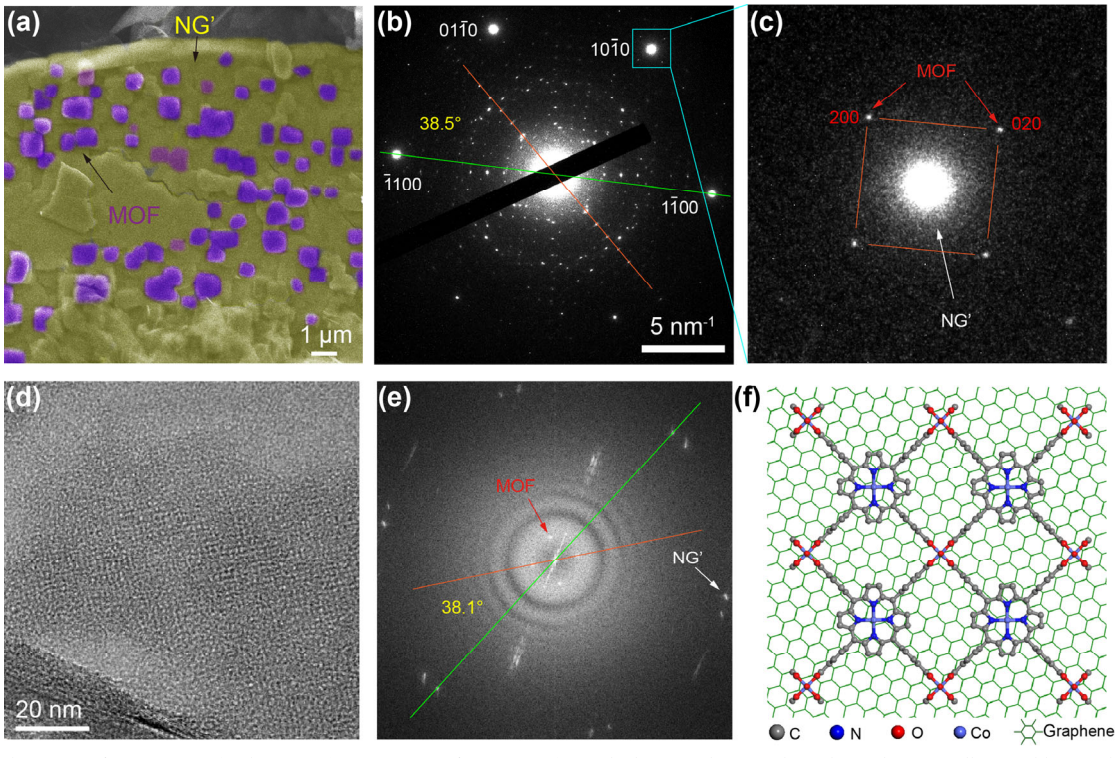

Figure 3 Alignment of MOF on **NG'** substrate. (a) SEM image of **MOF@NG'**, in which MOF sheets and graphene sheets are illustrated by purple and yellow, respectively. (b) SAED of **MOF@NG'**, the intersected angle between MOF (guided by orange line) and **NG'** (guided by green line) is ~38.5°. (c) Magnified diffraction pattern of the cyan squared region showing tetragonal secondary diffraction points of MOF around one spot belongs to **NG'**. (d) High-resolution TEM image of **MOF@NG'** displaying tetragonal lattice fringes of MOF. (e) FFT of the whole region also showing both sets of diffraction patterns of MOF and NG', the intersection angle is 38.1°. (f) Proposed unit cell matching for the alignment between MOF and graphene. Grey, blue, red, purple spheres represent carbon, nitrogen, oxygen, and cobalt atoms, respectively. Green hexagonal frames represent graphene.

3 Conclusion

In summary, through tailoring the structure of graphene substrate in terms of their sizes and nitrogen functionality, docking alignment of MOF can be therefore controlled, and their ORR performance can be ultimately tuned in terms of their reaction kinetics, catalytic pathway, peroxide production selectivity and catalytic turnover. The interfacial alignment has overcome the ultra large lattice mismatch and symmetry mismatch, leading to a promoted dispersity of electronic states of the active centers, which preferentially ferry 2.24 electrons to O_2 and results in a high peroxide selectivity up to 93.4%. The new dimension of tuneability in both meso-scale structures and ORR performances, as well as the high peroxide selectivity comparable to the concurrent widely used anthraquinone oxidation (AO) method, rendering the MOF-graphene nanocomposites a new class of promising electrocatalyst for mild H_2O_2 production and other industrial on-site applications.

4 Experimental

4.1 Synthesis of MOF@NG′

Few-layer graphene is synthesized through electrochemical exfoliation in two-electrode configuration with slight modification to previous reports [88]. The exfoliated graphene sheets were then ultrasonicated by a high-power ultrasonic probe (20 kHz, 120 W, Fisher Scientific) until a fully dispersed solution at a concentration of 2 mg·mL^{-1} is obtained. Then, TCPP (23.7 mg, 0.03 mmol) was dissolved in the graphene-DMF solution. The mixture was heated under refluxing condition for 20 h under N_2 protection, and then was cooled down to room temperature. $Co(NO_3)_2{\cdot}6H_2O$ (23.7 mg, 0.03 mmol) was further added into the solution and sonicated for another 15 min. The resulting mixture was transferred to a 10 mL Teflon-lined stainless-steel autoclave and kept at 80 °C for 72 h. After cooling down to room temperature at a ramping rate of 0.05 °C·min^{-1}, the precipitates in the autoclave were collected and washed by ethanol for three times. The product was dried under vacuum and denoted as **MOF@NG′**. Detailed synthesis protocol of MOF-graphene composites as control samples were described in the ESM.

4.2 Structural characterizations

The morphology of as-synthesized material is characterized by SEM (Phenom Pro and JEOL 7800F Prime) at various acceleration voltages. The crystallinity information was characterized by PXRD (Bruker D8 advance) using Cu Kα at λ = 0.15406 nm. Selected area electron diffraction and 3-D electron diffraction was characterized by TEM (JEOL 2100 Plus) using amorphous carbon grid. Spherical aberration transmission electron microscopy and electron energy loss spectroscopy (EELS) inspection was performed by using a cold FEG JEOL Grand-ARM 300F, which was operated at 300 and 80 kV. XPS (Kratos Analytical) is adopted to characterize the chemical states of C, O, N, Co elements of the as-synthesized materials. Inductively coupled plasma optical emission spectrometry (ICP-OES, ThermoFisher iCAP 7000) is used to quantitatively determine the amount of Co in each sample. All samples are firstly digested by concentrated nitric acid (guaranteed reagent). After that, sample solutions are prepared by diluting with 1% nitric acid and stored at 4 °C. Atomic force microscopy (AFM, Bruker Fastscan/ ICON) is used to investigate the thickness of **EG**, **NG**. Samples are firstly dispersed in DMF. The as-formed dispersion is drop casted onto Si substrate and dried under N_2 flow. Raman spectroscopy (Renishaw, Invia) is used to investigate vibrational state in the material with the laser power setting at 5%. N_2 adsorption/desorption isotherm of MOF-graphene nanocomposites are characterized using Quadrasorb under 77 K.

4.3 Electrochemical measurements

CV, electrochemical impedance spectroscopy (EIS), and chronocoulometry are conducted on an electrochemical workstation (CH Instrument, CHI660E) with a three-electrode configuration. Polarization curves and hydro-dynamic voltammetry are conducted on a bipotentiostat (CH Instrument, CHI760D) and analytical rotator (PINE instrument) with a three-electrode configuration. Catalysts modified glassy carbon (GC, 0.0707 cm^2) electrode is used as the working electrode. Ag/AgCl filled with saturated KCl solution is used as reference electrode, and Pt wire is the counter electrode, respectively. Detailed electrode preparation protocol for electrochemical characterization are provided in the ESM.

4.4 Constant potential production of H_2O_2

Constant potential electrolysis of O_2 is conducted in a home-made H-type electrochemical cell. The cathodic and anodic compartment is separated by Nafion-117 membrane (Dupont). Both chambers were filled with 0.5 M H_2SO_4 as the electrolyte solution. GC plate with an area of 1.0 cm ×1.0 cm is used as working electrode to support the catalysts. Ag/AgCl filled with saturated KCl solution is used as the reference electrode while Pt foil with an area of 2 cm^2 is used as the counter electrode. Prior to electrolysis, the GC plate is polished sequentially by 1.0, 0.3, and 0.05 μm alumina powder. For modification, 30 μL dispersed catalyst ink is drop-casted onto the glassy carbon plate and was dried under gentle N_2 flow. The modified GC plate is connected to a copper wire and sealed with silicone glue to prevent it from exposure in the electrolyte. High purity O_2 (99.99%) is purged into the electrolyte for at least 20 min to completely expel impurity gases. During electrolysis, potentials are kept at 0.4 V (vs. RHE) for 6 h. At certain time interval, 100 μL of the sample aliquots is taken from the cathode chamber and diluted by another 900 μL 0.1 M sodium acetate solution. The concentration hydrogen peroxide is then determined using Merck peroxide test kit.

Acknowledgements

This work is supported by the National Natural Science Foundation of China (Nos. 21522105 and 51861145313) and the Science & Technology Commission of Shanghai Municipality (17JC1404000). We acknowledge the support from the ShanghaiTech-SARI Joint Laboratory of Low-Carbon Energy Science, the Centre for High-resolution Electron Microscopy (ChEM, contract No. EM02161943), and the Analytical Instrumentation Center (Contract no. SPST-AIC10112914), SPST, ShanghaiTech University. The synchrotron X-ray portions of this research were carried out at the Stanford Synchrotron Radiation Lightsource, a Directorate of SLAC National Accelerator Laboratory and an Office of Science User Facility operated for the US Department of Energy Office of Science by Stanford University. L. M. and F. L. acknowledge Department of Chemistry Startup fund at Virginia Tech; A. M. acknowledge the support of National Natural Science Foundation of China (Nos. 21850410448 and 21835002). We thank the STEM support from Dr. Weiyan Liu in ChEM. We also thank Prof. O. Terasaki, Prof. Z. Liu, Prof. Y. Ma, and Mr. T. Sun for their guidance in electron diffraction and XPS analyses. We thank and will remember Prof. Frank Tsung for his kind

suggestion and encouragement, who left us forever on January 5, 2021 due to COVID-19.

Electronic Supplementary Material: Supplementary material (synthesis protocols for control samples, morphological and structural characterizations, porosity, electrochemical properties and activities including SEM, TEM, XPS, Raman, AFM investigations) is available in the online version of this article at https://doi.org/10.1007/s12274-021-3382-3.

References

[1] Campos-Martin, J. M.; Blanco-Brieva, G.; Fierro, J. L. G. Hydrogen peroxide synthesis: An outlook beyond the anthraquinone process. *Angew. Chem., Int. Ed.* **2006**, *45*, 6962–6984.

[2] Wang, K.; Huang, J. H.; Chen, H. X.; Wang, Y.; Song, S. Q. Recent advances in electrochemical 2e oxygen reduction reaction for on-site hydrogen peroxide production and beyond. *Chem. Commun.* **2020**, *56*, 12109–12121.

[3] Xia, C.; Xia, Y.; Zhu, P.; Fan, L.; Wang, H. T. Direct electrosynthesis of pure aqueous H_2O_2 solutions up to 20% by weight using a solid electrolyte. *Science* **2019**, *366*, 226–231.

[4] Perry, S. C.; Pangotra, D.; Vieira, L.; Csepei, L. I.; Sieber, V.; Wang, L.; de León, C. P.; Walsh, F. C. Electrochemical synthesis of hydrogen peroxide from water and oxygen. *Nat. Rev. Chem.* **2019**, *3*, 442–458.

[5] Jiang, K.; Zhao, J. J.; Wang, H. T. Catalyst design for electrochemical oxygen reduction toward hydrogen peroxide. *Adv. Funct. Mater.* **2020**, *30*, 2003321.

[6] Siahrostami, S.; Villegas, S. J.; Mostaghimi, A. H. B.; Back, S.; Farimani, A. B.; Wang, H. T.; Persson, K. A.; Montoya, J. A review on challenges and successes in atomic-scale design of catalysts for electrochemical synthesis of hydrogen peroxide. *ACS Catal.* **2020**, *10*, 7495–7511.

[7] Stamenkovic, V. R.; Strmcnik, D.; Lopes, P. P.; Markovic, N. M. Energy and fuels from electrochemical interfaces. *Nat. Mater.* **2017**, *16*, 57–69.

[8] Seh, Z. W.; Kibsgaard, J.; Dickens, C. F.; Chorkendorff, I.; Nørskov, J. K.; Jaramillo, T. F. Combining theory and experiment in electrocatalysis: Insights into materials design. *Science* **2017**, *355*, eaad4998.

[9] Luo, M. C.; Guo, S. J. Strain-controlled electrocatalysis on multimetallic nanomaterials. *Nat. Rev. Mater.* **2017**, *2*, 17059.

[10] Escudero-Escribano, M.; Malacrida, P.; Hansen, M. H.; Vej-Hansen, U. G.; Velázquez-Palenzuela, A.; Tripkovic, V.; Schiøtz, J.; Rossmeisl, J.; Stephens, I. E. L.; Chorkendorff, I. Tuning the activity of Pt alloy electrocatalysts by means of the lanthanide contraction. *Science* **2016**, *352*, 73–76.

[11] Gong, K. P.; Du, F.; Xia, Z. H.; Durstock, M.; Dai, L. M. Nitrogen-doped carbon nanotube arrays with high electrocatalytic activity for oxygen reduction. *Science* **2009**, *323*, 760–764.

[12] Chen, G. X.; Xu, C. F.; Huang, X. Q.; Ye, J. Y.; Gu, L; Li, G.; Tang, Z. C.; Wu, B. H.; Yang, H. Y.; Zhao, Z. P. et al. Interfacial electronic effects control the reaction selectivity of platinum catalysts. *Nat. Mater.* **2016**, *15*, 564–569.

[13] Zheng, Y.; Zheng, S. S.; Xue, H. G.; Pang, H. Metal-organic frameworks/graphene-based materials: Preparations and applications. *Adv. Funct. Mater.* **2018**, *28*, 1804950.

[14] Sangwan, V. K.; Beck, M. E.; Henning, A.; Luo, J. J.; Bergeron, H.; Kang, J. M.; Balla, I.; Inbar, H.; Lauhon, L. J.; Hersam, M. C. Self-aligned van der Waals heterojunction diodes and transistors. *Nano Lett.* **2018**, *18*, 1421–1427.

[15] Zhu, X. Y.; Monahan, N. R.; Gong, Z. Z.; Zhu, H. M.; Williams, K. W.; Nelson, C. A. Charge transfer excitons at van der Waals interfaces. *J. Am. Chem. Soc.* **2015**, *137*, 8313–8320.

[16] Cheng, R.; Li, D. H.; Zhou, H. L.; Wang, C.; Wang, A. X.; Jiang, S.; Liu, Y.; Chen, Y.; Huang, Y.; Duan, X. F. Electroluminescence and photocurrent generation from atomically sharp WSe_2/MoS_2 heterojunction p–n diodes. *Nano Lett.* **2014**, *14*, 5590–5597.

[17] Su, J.; Li, G. D.; Li, X. H.; Chen, J. S. 2D/2D heterojunctions for catalysis. *Adv. Sci.* **2019**, *6*, 1801702.

[18] Popp, T. M. O.; Yaghi, O. M. Sequence-dependent materials. *Acc. Chem. Res.* **2017**, *50*, 532–534.

[19] Pomerantseva, E.; Gogotsi, Y. Two-dimensional heterostructures for energy storage. *Nat. Energy* **2017**, *2*, 17089.

[20] Furukawa, H.; Cordova, K. E.; O'Keeffe, M.; Yaghi, O. M. The chemistry and applications of metal-organic frameworks. *Science* **2013**, *341*, 1230444.

[21] Islamoglu, T.; Goswami, S.; Li, Z. Y.; Howarth, A. J.; Farha, O. K.; Hupp, J. T. Postsynthetic tuning of metal–organic frameworks for targeted applications. *Acc. Chem. Res.* **2017**, *50*, 805–813.

[22] Ding, Y. J.; Chen, Y. P.; Zhang, X. L.; Chen, L.; Dong, Z. H.; Jiang, H. L.; Xu, H. X.; Zhou, H. C. Controlled intercalation and chemical exfoliation of layered metal–organic frameworks using a chemically labile intercalating agent. *J. Am. Chem. Soc.* **2017**, *139*, 9136–9139.

[23] Jiang, H. Q.; Liu, X. C.; Wu, Y. S.; Shu, Y. F.; Gong, X.; Ke, F. S.; Deng, H. X. Metal-organic frameworks for high charge-discharge rates in lithium-sulfur batteries. *Angew. Chem., Int. Ed.* **2018**, *57*, 3916–3921.

[24] Dai, H. M.; Sun, J.; Zhou, Y.; Zhou, Z. R.; Luo, W.; Wei, G. F.; Deng, H. X. Reticulation of 2D semiconductors by metal–organic approach for efficient hydrogen evolution. *ACS Sustainable Chem. Eng.* **2020**, *8*, 8102–8110.

[25] Lu, X. F.; Liao, P. Q.; Wang, J. W.; Wu, J. X.; Chen, X. W.; He, C. T.; Zhang, J. P.; Li, G. R.; Chen, X. M. An alkaline-stable, metal hydroxide mimicking metal-organic framework for efficient electrocatalytic oxygen evolution. *J. Am. Chem. Soc.* **2016**, *138*, 8336–8339.

[26] Lu, X. F.; Xia, B. Y.; Zang, S. Q.; Lou, X. W. Metal-organic frameworks based electrocatalysts for the oxygen reduction reaction. *Angew. Chem., Int. Ed.* **2020**, *59*, 4634–4650.

[27] Shekhah, O.; Liu, J.; Fischer, R. A.; Wöll, C. MOF thin films: Existing and future applications. *Chem. Soc. Rev.* **2011**, *40*, 1081–1106.

[28] Shekhah, O.; Wang, H.; Paradinas, M.; Ocal, C.; Schüpbach, B.; Terfort, A.; Zacher, D.; Fischer, R. A.; Wöll, C. Controlling interpenetration in metal–organic frameworks by liquid-phase epitaxy. *Nat. Mater.* **2009**, *8*, 481–484.

[29] Hu P.; Zhuang, J.; Chou, L. Y.; Lee, H. K.; Ling, X. Y.; Chuang, Y. C.; Tsung, C. K. Surfactant-directed atomic to mesoscale alignment: Metal nanocrystals encased individually in single-crystalline porous nanostructures. *J. Am. Chem. Soc.* **2014**, *136*, 10561–10564.

[30] Zhao, Y. B.; Kornienko, N.; Liu, Z.; Zhu, C. H.; Asahina, S.; Kuo, T. R.; Bao, W.; Xie, C. L.; Hexemer, A.; Terasaki, O. et al. Mesoscopic constructs of ordered and oriented metal–organic frameworks on plasmonic silver nanocrystals. *J. Am. Chem. Soc.* **2015**, *137*, 2199–2202.

[31] Falcaro, P.; Okada, K.; Hara, T.; Ikigaki, K.; Tokudome, Y.; Thornton, A. W.; Hill, A. J.; Williams, T.; Doonan, C.; Takahashi, M. Centimetre-scale micropore alignment in oriented polycrystalline metal–organic framework films via heteroepitaxial growth. *Nat. Mater.* **2017**, *16*, 342–348.

[32] Wu, J. X.; Hou, S. Z.; Zhang, X. D.; Xu, M.; Yang, H. F.; Cao, P. S.; Gu, Z. Y. Cathodized copper porphyrin metal–organic framework nanosheets for selective formate and acetate production from CO_2 electroreduction. *Chem. Sci.* **2019**, *10*, 2199–2205.

[33] Zhao, M. T.; Huang, Y.; Peng, Y. W.; Huang, Z. Q.; Ma, Q. L.; Zhang, H. Two-dimensional metal–organic framework nanosheets: Synthesis and applications. *Chem. Soc. Rev.* **2018**, *47*, 6267–6295.

[34] Zagal, J. H.; Koper, M. T. M. Reactivity descriptors for the activity of molecular MN_4 catalysts for the oxygen reduction reaction. *Angew. Chem., Int. Ed.* **2016**, *55*, 14510–14521.

[35] Lu, Z. Y.; Chen, G. X.; Siahrostami, S.; Chen, Z. H.; Liu, K.; Xie, J.; Liao, L.; Wu, T.; Lin, D. C.; Liu, Y. Y. et al. High-efficiency oxygen reduction to hydrogen peroxide catalysed by oxidized carbon materials. *Nat. Catal.* **2018**, *1*, 156–162.

[36] Han, L.; Sun, Y. Y.; Li, S.; Cheng, C.; Halbig, C. E.; Feicht, P.; Hübner, J. L.; Strasser, P.; Eigler, S. In-plane carbon lattice-defect regulating electrochemical oxygen reduction to hydrogen peroxide production over nitrogen-doped graphene. *ACS Catal.* **2019**, *9*, 1283–1288.

[37] Chen, S. C.; Chen, Z. H.; Siahrostami, S.; Higgins, D.; Nordlund, D.; Dimosthenis, S.; Kim, T. R.; Liu, Y. Z.; Yan, X. Z.; Nilsson, E. et al. Designing boron nitride islands in carbon materials for efficient electrochemical synthesis of hydrogen peroxide. *J. Am. Chem. Soc.* **2018**, *140*, 7851–7859.

[38] Tan, Y. M.; Xu, C. F.; Chen, G. X.; Fang, X. L.; Zheng, N. F.; Xie, Q. J. Facile synthesis of manganese-oxide-containing mesoporous nitrogen-doped carbon for efficient oxygen reduction. *Adv. Funct. Mater.* **2012**, *22*, 4584–4591.

[39] Valarselvan, S.; Manisankar, P. Electrocatalytic reduction of oxygen at glassy carbon electrode modified by polypyrrole/anthraquinones composite film in various pH media. *Electrochim. Acta* **2011**, *56*, 6945–6953.

[40] Ohnishi, R.; Katayama, M.; Cha, D.; Takanabe, K.; Kubota, J.; Domen, K. Titanium nitride nanoparticle electrocatalysts for oxygen reduction reaction in alkaline solution. *J. Electrochem. Soc.* **2013**, *160*, F501.

[41] Yasuda, S.; Yu, L.; Kim, J.; Murakoshi, K. Selective nitrogen doping in graphene for oxygen reduction reactions. *Chem. Commun.* **2013**, *49*, 9627–9629.

[42] Aijaz, A.; Fujiwara, N.; Xu, Q. From metal–organic framework to nitrogen-decorated nanoporous carbons: High CO_2 uptake and efficient catalytic oxygen reduction. *J. Am. Chem. Soc.* **2014**, *136*, 6790–6793.

[43] Choi, C. H.; Kwon, H. C.; Yook, S.; Shin, H.; Kim, H.; Choi, M. Hydrogen peroxide synthesis via enhanced two-electron oxygen reduction pathway on carbon-coated Pt Surface. *J. Phys. Chem. C* **2014**, *118*, 30063–30070.

[44] Park, J.; Nabae, Y.; Hayakawa, T.; Kakimoto, M. A. Highly selective two-electron oxygen reduction catalyzed by mesoporous nitrogen-doped carbon. *ACS Catal.* **2014**, *4*, 3749–3754.

[45] Vikkisk, M.; Kruusenberg, I.; Joost, U.; Shulga, E.; Kink, I.; Tammeveski, K. Electrocatalytic oxygen reduction on nitrogen-doped graphene in alkaline media. *Appl. Catal. B: Environ.* **2014**, *147*, 369–376.

[46] Wang, H.; Yin, F. X.; Li, G. R.; Chen, B. H.; Wang, Z. Q. Preparation, characterization and bifunctional catalytic properties of MOF(Fe/Co) catalyst for oxygen reduction/evolution reactions in alkaline electrolyte. *Int. J. Hydrogen Energy* **2014**, *39*, 16179–16186.

[47] Favaro, M.; Ferrighi, L.; Fazio, G.; Colazzo, L.; Di Valentin, C.; Durante, C.; Sedona, F.; Gennaro, A.; Agnoli, S.; Granozzi, G. Single and multiple doping in graphene quantum dots: Unraveling the origin of selectivity in the oxygen reduction reaction. *ACS Catal.* **2015**, *5*, 129–144.

[48] Rameshkumar, P.; Praveen, R.; Ramaraj, R. Electroanalysis of oxygen reduction and formic acid oxidation using reduced graphene oxide/gold nanostructures modified electrode. *J. Electroanal. Chem.* **2015**, *754*, 118–124.

[49] Rigsby, M. L.; Wasylenko, D. J.; Pegis, M. L.; Mayer, J. M. Medium effects are as important as catalyst design for selectivity in electrocatalytic oxygen reduction by iron–porphyrin complexes. *J. Am. Chem. Soc.* **2015**, *137*, 4296–4299.

[50] Wu, J. J.; Zhang, D.; Niwa, H.; Harada, Y.; Oshima, M.; Ofuchi, H.; Nabae, Y.; Okajima, T.; Ohsaka, T. Enhancement in kinetics of the oxygen reduction reaction on a nitrogen-doped carbon catalyst by introduction of iron via electrochemical methods. *Langmuir* **2015**, *31*, 5529–5536.

[51] Fellinger, T. P.; Hasché, F.; Strasser, P.; Antonietti, M. Mesoporous Nitrogen-doped carbon for the electrocatalytic synthesis of hydrogen peroxide. *J. Am. Chem. Soc.* **2012**, *134*, 4072–4075.

[52] Li, B. Q.; Zhao, C. X.; Liu, J. N.; Zhang, Q. Electrosynthesis of hydrogen peroxide synergistically catalyzed by atomic Co–N_x–C sites and oxygen functional groups in noble-metal-free electrocatalysts. *Adv. Mater.* **2019**, *31*, 1808173.

[53] Jung, E.; Shin, H.; Lee, B. H.; Efremov, V.; Lee, S.; Lee, H. S.; Kim, J.; Antink, W. H.; Park, S.; Lee, K. S. et al. Atomic-level tuning of Co–N–C catalyst for high-performance electrochemical H_2O_2 production. *Nat. Mater.* **2020**, *19*, 436–442.

[54] Sun, Y. Y.; Silvioli, L.; Sahraie, N. R.; Ju, W.; Li, J. K.; Zitolo, A.; Li, S.; Bagger, A.; Arnarson, L.; Wang, X. L. et al. Activity–selectivity trends in the electrochemical production of hydrogen peroxide over single-site metal–nitrogen–carbon catalysts. *J. Am. Chem. Soc.* **2019**, *141*, 12372–12381.

[55] Wang, M. J.; Zhang, N.; Feng, Y. G.; Hu, Z. W.; Shao, Q.; Huang, X. Q. Partially pyrolyzed binary metal-organic framework nanosheets for efficient electrochemical hydrogen peroxide synthesis. *Angew. Chem., Int. Ed.* **2020**, *59*, 14373–14377.

[56] Byeon, A.; Cho, J.; Kim, J. M.; Chae, K. H.; Park, H. Y.; Hong, S. W.; Ham, H. C.; Lee, S. W.; Yoon, K. R.; Kim, J. Y. High-yield electrochemical hydrogen peroxide production from an enhanced two-electron oxygen reduction pathway by mesoporous nitrogen-doped carbon and manganese hybrid electrocatalysts. *Nanoscale Horiz.* **2020**, *5*, 832–838.

[57] Sun, Y. Y.; Sinev, I.; Ju, W.; Bergmann, A.; Dresp, S.; Kühl, S.; Spöri, C.; Schmies, H.; Wang, H.; Bernsmeier, D. et al. Efficient electrochemical hydrogen peroxide production from molecular oxygen on nitrogen-doped mesoporous carbon catalysts. *ACS Catal.* **2018**, *8*, 2844–2856.

[58] Sun, Y. Y.; Li, S.; Jovanov, Z. P.; Bernsmeier, D.; Wang, H.; Paul, B.; Wang, X. L.; Kühl, S.; Strasser, P. Structure, activity, and faradaic efficiency of nitrogen-doped porous carbon catalysts for direct electrochemical hydrogen peroxide production. *ChemSusChem* **2018**, *11*, 3388–3395.

[59] Liu, M. H.; Zhang, H.; Li, Y. L.; Su, H.; Zhou, W. L.; Zhao, X.; Cheng, W. R.; Liu, Q. H. Crystallinity dependence for high-selectivity electrochemical oxygen reduction to hydrogen peroxide. *Chem. Commun.* **2020**, *56*, 5299–5302.

[60] Li, L. Q.; Tang, C.; Zheng, Y.; Xia, B. Q.; Zhou, X. L.; Xu, H. L.; Qiao, S. Z. Tailoring selectivity of electrochemical hydrogen peroxide generation by tunable pyrrolic-nitrogen-carbon. *Adv. Energy Mater.* **2020**, *10*, 2000789.

[61] Ko, Y. J.; Choi, K.; Yang, B.; Lee, W. H.; Kim, J. Y.; Choi, J. W.; Chae, K. H.; Lee, J. H.; Hwang, Y. J.; Min, B. K. et al. A catalyst design for selective electrochemical reactions: Direct production of hydrogen peroxide in advanced electrochemical oxidation. *J. Mater. Chem. A* **2020**, *8*, 9859–9870.

[62] Dong, Y. Q.; Su, J. X.; Zhou, S. Q.; Wang, M.; Huang, S. P.; Lu, C. H.; Yang, H. B.; Fu, F. F. Carbon-based dots for the electrochemical production of hydrogen peroxide. *Chem. Commun.* **2020**, *56*, 7609–7612.

[63] Zhao, X.; Wang, Y.; Da, Y. L.; Wang, X. X.; Wang, T. T.; Xu, M. Q.; He, X. Y.; Zhou, W.; Li, Y. F.; Coleman, J. N. et al. Selective electrochemical production of hydrogen peroxide at zigzag edges of exfoliated molybdenum telluride nanoflakes. *Natl. Sci. Rev.* **2020**, *7*, 1360–1366.

[64] Kim, H. W.; Ross, M. B.; Kornienko, N.; Zhang, L.; Guo, J. H.; Yang, P. D.; McCloskey, B. D. Efficient hydrogen peroxide generation using reduced graphene oxide-based oxygen reduction electrocatalysts. *Nat. Catal.* **2018**, *1*, 282–290.

[65] Sa, Y. J.; Kim, J. H.; Joo, S. H. Active edge-site-rich carbon nanocatalysts with enhanced electron transfer for efficient electrochemical hydrogen peroxide production. *Angew. Chem., Int. Ed.* **2019**, *58*, 1100–1105.

[66] Zhao, K.; Su, Y.; Quan, X.; Liu, Y. M.; Chen, S.; Yu, H. T. Enhanced H_2O_2 production by selective electrochemical reduction of O_2 on fluorine-doped hierarchically porous carbon. *J. Catal.* **2018**, *357*, 118–126.

[67] Iglesias, D.; Giuliani, A.; Melchionna, M.; Marchesan, S.; Criado, A.; Nasi, L.; Bevilacqua, M.; Tavagnacco, C.; Vizza, F.; Prato, M. et al. N-doped graphitized carbon nanohorns as a forefront electrocatalyst in highly selective O_2 reduction to H_2O_2. *Chem* **2018**, *4*, 106–123.

[68] Pham-Truong, T. N.; Petenzi, T.; Ranjan, C.; Randriamahazaka, H.; Ghilane, J. Microwave assisted synthesis of carbon dots in ionic liquid as metal free catalyst for highly selective production of hydrogen peroxide. *Carbon* **2018**, *130*, 544–552.

[69] Lim, B.; Jiang, M. J.; Camargo, P. H. C.; Cho, E. C.; Tao, J.; Lu, X. M.; Zhu, Y. M.; Xia, Y. N. Pd-Pt bimetallic nanodendrites with high activity for oxygen reduction. *Science* **2009**, *324*, 1302–1305.

[70] Wang, D. L.; Xin, H. L.; Hovden, R.; Wang, H.; Yu, Y. C.; Muller, D. A.; DiSalvo, F. J.; Abruña, H. D. Structurally ordered intermetallic platinum-cobalt core-shell nanoparticles with enhanced activity and stability as oxygen reduction electrocatalysts. *Nat. Mater.* **2013**, *12*, 81–87.

[71] Xie, S. F.; Choi, S. I.; Lu, N.; Roling, L. T.; Herron, J. A.; Zhang, L.; Park, J.; Wang, J. G.; Kim, M. J.; Xie, Z. X. et al. Atomic layer-by-layer deposition of Pt on Pd nanocubes for catalysts with enhanced activity and durability toward oxygen reduction. *Nano Lett.* **2014**, *14*, 3570–3576.

[72] Yang, J. H.; Yang, J.; Ying, J. Y. Morphology and lateral strain control of Pt nanoparticles via core–shell construction using alloy AgPd Core

toward oxygen reduction reaction. *ACS Nano* **2012**, *6*, 9373–9382.
[73] Laokroekkiat, S.; Hara, M.; Nagano, S.; Nagao, Y. Metal-organic coordination network thin film by surface-induced assembly. *Langmuir* **2016**, *32*, 6648–6655.
[74] Lukasczyk, T.; Flechtner, K.; Merte, L. R.; Jux, N.; Maier, F.; Gottfried, J. M.; Steinrück, H. P. Interaction of cobalt(II) tetraarylporphyrins with a Ag(111) surface studied with photoelectron spectroscopy. *J. Phys. Chem. C* **2007**, *111*, 3090–3098.
[75] Kumar, P.; Kumar, A.; Sreedhar, B.; Sain, B.; Ray, S. S.; Jain, S. L. Cobalt phthalocyanine immobilized on graphene oxide: An efficient visible-active catalyst for the photoreduction of carbon dioxide. *Chem.–Eur. J.* **2014**, *20*, 6154–6161.
[76] Malig, J.; Jux, N.; Kiessling, D.; Cid, J. J.; Vazquez, P.; Torres, T.; Guldi, M. D. Towards tunable graphene/phthalocyanine-PPV hybrid systems. *Angew. Chem., Int. Ed.* **2011**, *50*, 3561–3565.
[77] Pham, V. D.; Lagoute, J.; Mouhoub, O.; Joucken, F.; Repain, V.; Chacon, C.; Bellec, A.; Girard, Y.; Rousset, S. Electronic interaction between nitrogen-doped graphene and porphyrin molecules. *ACS Nano* **2014**, *8*, 9403–9409.
[78] Wojcik, A.; Kamat, P. V. Reduced graphene oxide and porphyrin. An interactive affair in 2-D. *ACS Nano* **2010**, *4*, 6697–6706.
[79] Sharoyan, E. G.; Sharoyan, V. E.; Ovsyannikov, M. EXAFS studies of organic molecular ferromagnets based on cobalt phthalocyanine: $Na_{2.8}$CoPc. *J. Porphyr. Phthalocyanines* **1998**, *2*, 237–241.
[80] Sarangi, R.; Cho, J.; Nam, W.; Solomon, E. I. XAS and DFT investigation of mononuclear cobalt(III) peroxo complexes: Electronic control of the geometric structure in CoO_2 versus NiO_2 systems. *Inorg. Chem.* **2011**, *50*, 614–620.
[81] Zhang, Q. R.; Tan, X.; Bedford, N. M.; Han, Z. J.; Thomsen, L.; Smith, S.; Amal, R.; Lu, X. Y. Direct insights into the role of epoxy groups on cobalt sites for acidic H_2O_2 production. *Nat. Commun.* **2020**, *11*, 4181.
[82] Wang, Y. H.; Wang, X. T.; Ze, H. J.; Zhang, X. G.; Radjenovic, P. M.; Zhang, Y. J.; Dong, J. C.; Tian, Z. Q.; Li, J. F. Spectroscopic verification of adsorbed hydroxy intermediates in the bifunctional mechanism of the hydrogen oxidation reaction. *Angew. Chem., Int. Ed.*, in press, DOI: 10.1002/anie.202015571.
[83] Hu, A. Q.; Pang, Q. Q.; Tang, C.; Bao, J. X.; Liu, H. Q.; Ba, K.; Xie, S. H.; Chen, J.; Chen, J. H.; Yue, Y. W. et al. Epitaxial growth and integration of insulating metal–organic frameworks in electrochemistry. *J. Am. Chem. Soc.* **2019**, *141*, 11322–11327.
[84] Wu, J.; Chen, J. H.; Wang, C.; Zhou, Y.; Ba, K.; Xu, H.; Bao, W. Z.; Xu, X. H.; Carlsson, A.; Lazar, S. et al. Metal–organic framework for transparent electronics. *Adv. Sci.* **2020**, *7*, 1903003.
[85] Kumar, A.; Banerjee, K.; Foster, A. S.; Liljeroth, P. Two-dimensional band structure in honeycomb metal–organic frameworks. *Nano Lett.* **2018**, *18*, 5596–5602.
[86] Lai, L. F.; Potts, J. R.; Zhan, D.; Wang, L.; Poh, C. K.; Tang, C. H.; Gong, H.; Shen, Z. X.; Lin, J. Y.; Ruoff, R. S. Exploration of the active center structure of nitrogen-doped graphene-based catalysts for oxygen reduction reaction. *Energy Environ. Sci.* **2012**, *5*, 7936–7942.
[87] Xing T.; Zheng, Y.; Li, L. H.; Cowie, B. C. C.; Gunzelmann, D.; Qiao, S. Z.; Huang, S. M.; Chen, Y. Observation of active sites for oxygen reduction reaction on nitrogen-doped multilayer graphene. *ACS Nano* **2014**, *8*, 6856–6862.
[88] Parvez, K.; Wu, Z. S.; Li, R. J.; Liu, X. J.; Graf, R.; Feng, X. L. Müllen, K. Exfoliation of graphite into graphene in aqueous solutions of inorganic salts. *J. Am. Chem. Soc.* **2014**, *136*, 6083–6091.